Supplementary Information

Maximization of Hydrogen Peroxide Utilization in Proton Exchange Membrane H_2O_2 Electrolyzer for Efficient Power-to-Hydrogen Conversion

Jie Yang,[a,b] *Ruimin Ding,* [*a] *Chang Liu,*[a,c] *Lifang Chen,*[a] *Qi wang,* [a,b] *Shanshan Liu,*[a] *Qinchao Xu,*[a] *Xi Yin,*[*a]

[a] State Key Laboratory of Coal Conversion, Institute of Coal Chemistry, Chinese Academy of Sciences; Taiyuan, Shanxi 030001, China.

[b] School of Chemical Engineering, University of Chinese Academy of Sciences; Beijing 100049, China.

[c] Center of Materials Science and Optoelectronics Engineering, University of Chinese Academy of Sciences; Beijing 100049, China

*Corresponding author. Email: dingrm@sxicc.ac.cn, xiyin@sxicc.ac.cn

Number of pages: 30

Number of figures: 16

Number of tables: 2

Experimental Sections

Materials

Cobalt chloride ($CoCl_2$, 99.7%, anhydrous, Aladdin Biochemical Technology Co.), iron(III) chloride ($FeCl_3$, 97%, anhydrous, Sigma Aldrich), aniline (98%, Sigma-Aldrich), H_2O_2 (30 wt%, Alfa Aesar), hydrochloric acid (HCl, 36–38 wt%, analytical reagent grade; SCR, China), nitric acid (HNO_3, 65–68 wt%, analytical reagent grade; SCR, China), APS (98%, Sigma-Aldrich), isopropanol (IPA, >99.7%, analytical reagent grade; Kermel, China), sulfuric acid (H_2SO_4, 95–98 wt%, analytical reagent grade; SCR, China), deionized water (DI-water, Milli-Q, 18.2 MΩ cm at 25°C), ultrapure N_2 (99.999%), ultrapure O_2 (99.999%), carbon black (BlackPearl 2000, Cabot Co.), 20 wt% Pt/C (Hispec3000, Johnson Matthey Co.) and a D521 Nafion dispersion (5 wt%, EW = 1100, Chemours) were utilized as received.

Preparation of the catalysts

The Co-N-C were synthesized using a method reported.[1, 2] Aniline (11 mmol), $CoCl_2$ (55 mmol), and oxidized carbon black (OCB, carbon black was pretreated in 70% nitric acid at 80 °C for 8 h, rinsed with DI-water and vacuum-dried at 80 °C) were prepared by polymerizing and concentrating a mixture of solutions to obtain a black slurry. The slurry was loaded into an alumina combustion boat and heat-treated at 900 °C in a tube furnace in N_2 at ambient pressure. The ramping rate was 30 °C/min, and the holding time at 900 °C was one hour. The pyrolyzed material was ground into

a fine powder using an agate mortar and pestle and treated with a 12 N HCl solution for 24 h to remove spectator Co-rich phases. The acid-leached sample was washed with DI-water, and dried under vacuum at 60 °C. The final product was obtained after the second heat treatment at 900 °C for 3 h in flowing N_2 with a ramping rate of 30 °C/min.

The Fe-N-C material was synthesized using the same procedure, but the $CoCl_2$ was replaced with iron chloride ($FeCl_3$).

Physical characterizations

The Co-N-C and Fe-N-C catalysts were characterized using a scanning electron microscope (SEM, JSM-7001F, Japan) operated at an accelerating voltage of 80 kV, the high-resolution transmission electron microscope (TEM, JEM-2100F, JEOL, Japan). An aberration-corrected high-angle annular dark-field scanning transmission electron microscope (HAADF-STEM, Titan Cubed Themis G2 300, FEI, USA) operated at an accelerating voltage of 300 kV. Powder X-ray diffraction (XRD, D8 ADVANCE A25, Bruker Co., USA) patterns were recorded using a Bruker D8-Advance-A25 diffractometer with Cu Kα radiation over a 2θ range from 5° to 90°. Raman spectra were recorded on a LabRAM HR Evolution (HORIBA Scientific, France) using a 514 nm laser as the excitation source. The X-ray photoelectron spectroscopy (XPS, Axis Ultra DLD, Kratos Analytical Ltd, UK) was performed on a monochromatic Al Kα source at 150 W without charge compensation.

Figure S1a, b shows the scanning electron microscopy (SEM) micrographs of the Co-N-C and the Fe-N-C catalyst, displaying a similar morphology in multilayer

graphene and irregular clusters. Introducing a different transition metal in the synthesis does not result in significant structural changes during pyrolysis. In particular, the transmission electron microscopy (TEM) image of the M-N-C catalyst confirms a homogeneous carbon nanostructure without any Co- or Fe-rich particles (**Figure S1c, d**). And the highly dispersed cobalt or iron atoms were observed in the sample using scanning TEM (STEM) in high-angle annular dark field imaging (HAADF) mode, which was distributed in the nitrogen-doped carbon matrix and represented by the bright spots (**Figure S1e, f**). The X-ray diffraction (XRD, **Figure S2a**) was performed to identify the presence of carbon- or metal-based crystalline structures. The two broad diffraction peaks observed for two catalysts at around 25° and 44° are assigned to the (002) and (101) planes of the graphite phase (PDF #75–1621). No characteristic peaks related to metal-rich phases could be observed, agreeing well with the TEM and HAADF-STEM results. The Raman spectra (**Figure S2b**) of the samples also show very similar patterns with two intense D- and G-band peaks at *ca*. 1350 cm^{-1} and 1590 cm cm^{-1}, respectively. Because the D-band is the characteristic peak of vacancies or defects in graphene, and the G band is the characteristic peak of graphitic layers, which arises from the E_{2g} vibrational mode in the D_{6h}^{4} symmetry group of the graphite crystal planes. The relative intensities of the D to G band for the two catalysts are almost identical, indicating that both catalysts have a highly similar disordered graphitic structure, which is also confirmed by the broad graphitic peaks in their XRD patterns. The compositions and electronic states of the two catalysts were then investigated using X-ray photoelectron spectroscopy (XPS). The carbon, nitrogen, and oxygen contents of

the two catalysts show very similar spectra and valence states (**Figure S2c**). The estimated atomic percentage contents of N in the Co-N-C and Fe-N-C catalysts were 3.73 and 4.79 at.%, respectively. Similar overall nitrogen content is observed in the different catalysts, whereas the metal contents in the Co-N-C and Fe-N-C catalysts range from 0.27 to 0.06 at.%, respectively. Moreover, the high-resolution N 1s XPS spectra of two catalysts (**Figure S2d**) can be fitted with the same set of five components assigned to different nitrogen electronic environments, including $N_{pyridinic}$ (398.4 eV), metal-coordinated M-N_x moieties (399.5 eV), $N_{pyrrolic}$ (401 eV), $N_{graphitic}$ (402.4 eV), as well as $N_{oxidized}$ (404.2 eV). Based on all characterizations, we infer that the Co-N-C and Fe-N-C catalysts possess similar physicochemical properties, differing only in the nature of the transition metal in the reactive sites.

Electrochemical measurements

The electrochemical measurements of HPOR activity were conducted in an H-type electrolysis cell by a Pine Research MSR rotator (Pine Research Instrumentation Co. Ltd.) and a bipotentiostat (CHI 760E, CH Instruments, Inc.). A proton exchange membrane (Nafion® NR211) was used to separate the two compartments of the H-cell. A glassy carbon electrode (GCE) (Φ = 5.00 mm, area = 0.196 cm^2, Pine Research Instrumentation Co. Ltd.) and an Ag/AgCl (KCl, 3 M) reference electrode were placed in one cell compartment filled with 0.5 M H_2SO_4 and 0.5 M H_2O_2. A graphite rod counter electrode was positioned in another compartment filled with 0.5 M H_2SO_4.

For Fe-N-C and Co-N-C catalysts, the corresponding catalyst inks were made by

ultrasonically dispersing 5 mg of the catalyst in a mixture of DI-water (500 μL), IPA (500 μL), and D521 Nafion dispersion (15 μL, 5 wt%) to form a homogeneous suspension. Then, 4.0 μL of the ink was deposited onto a GCE to form a uniform film with a catalyst loading of *ca*. 0.1 mg/cm^2.

For Pt-C catalyst inks were prepared by ultrasonically dispersing 5 mg of each catalyst in a mixture of DI-water (800 μL), IPA (200 μL), and D521 Nafion dispersion (10 μL, 5 wt%) to form a homogeneous suspension. Then, 4.0 μL of the ink was deposited onto a GCE to form a uniform film with a catalyst loading of *ca*. 0.1 mg/cm^2.

The HPOR performance was measured by cyclic voltammetry (CV) from 0 to 1.0 V *vs*. RHE in O_2-saturated 0.5 M H_2SO_4/0.5 M H_2O_2 solution. The scan rate was 50 mV/s, and the rotation rate was 900 rpm. The logarithm of current density (*j*) was plotted against the potential to obtain a semilogarithmic polarization curve, namely, the Tafel plot. The linear part of this curve was fitted using the equation:

$$\eta = a + b\log j \qquad Eq.S1$$

where η is the overpotential, a is the intercept at x-axis when $\eta = 0$, b is the Tafel slope, and j is the average of the forward and reverse scan current density in CV.

We conducted electrochemical HPOR and HPRR tests on a rotating disk electrode (RDE) at room temperature. In an O_2-saturated solution containing 0.5 M H_2O_2 and 0.5 M H_2SO_4 electrolyte, the cyclic CV curves of the three catalysts are presented in **Figure S3a, b.** The anodic current at high potential represents the HPOR-dominated process, the cathodic current at low potential represents the hydrogen peroxide reduction reaction (HPRR), and the oxygen reduction reaction (ORR) dominates the process. The

net current becomes zero at the mixed potential (U_{mix}) of the system when the anodic and cathodic processes are in equilibrium. For an ideal HPOR catalyst, the U_{mix} should be close to the thermodynamic equilibrium potential (0.704 V *vs*. RHE) to achieve high efficiency in HPOR. As displayed in **Figure S3c**, the Co-N-C, Fe–N–C, and Pt/C showed U_{mix} of *ca.* 0.71, 0.81, and 0.80 V *vs*. RHE, and maximum current density of *ca.* 375, 242, and 254 mA/cm^2 at 1.0 V *vs*. RHE, respectively. Furthermore, the calculated Tafel slope was 77.5 mV/dec for the Co-N-C catalyst based on the Tafel equation (*Eq*. S1), but the Tafel slope for the Fe-N-C and Pt-C catalysts cannot be fitted (**Figure S3d**). We consider that there are multiple competing reactions (HPOR, HPDR, and HPRR) in the U_{mix} interval, which lead to the oxidation currents obtained being a superpositions of multiple competing reactions.

Computational Details

Spin-polarized first-principles computations were performed using GGA-PBE functional[3] in the Vienna ab initio simulation package (VASP 5.4.1).[4, 5] The ion-electron interaction was described by the projector augmented wave (PAW) approach.[6, 7] A cut-off energy of 400 eV for the plane wave basis was used for all atoms relaxed. The van der Waals (vdW) interactions was expressed by Grimme's DFT-D3 method.[8] The k-point grids were set to be 4 × 4 × 1 by the Monkhorst–Pack method and force and energy convergence criterion were set to 0.01 eV/Å and 10^{-5} eV for all systems, respectively. The chemical potential of the H^+/e^- pair is equal to half of the gas-phase H_2 at standard hydrogen electrode (SHE) conditions from the computational hydrogen

electrode (CHE).[9] All free energies were calculated relative to H_2O(l) and H_2(g). To consider the solvation effect, we added a solvation correction (E_{sol}) of ~0.25 eV[10] to Pt and ~0.3 eV[11] to Fe-N-C for the adsorption free energies. Pt(111), Pt(100) and Pt(110) surface were constructed by a *p*(3×3) supercell. The Fe-N_4 site embedded in the *p*(4×6) graphene slab to build Fe-N-C surface. The vacuum was set to 15 Å for four slabs to avoid interactions. For Pt(111), Pt(100) and Pt(110) surface, the uppermost two layer were fully relaxed and the bottom two layer were fixed at the bulk.

The free energy for each reaction intermediate is calculated as:

$$G = E_{\mathrm{DFT}} + ZPE - TS + E_{sol} \qquad Eq.\ \mathrm{S2}$$

where E_{DFT} is the energy by DFT calculation, *ZPE* and *S* are the zero-point energy and the entropy, *T* is the temperature (298.15 K, in our work), and E_{sol} is the solvation correction. For adsorbed reaction intermediates, their ZPE and *S* are obtained via vibrational frequencies computations.

The binding free energy of HOO* intermediate ($\Delta G_{\mathrm{HOO*}}$, at *U* = 0 V vs. CHE) is defined as follow:

$$\Delta G_{\mathrm{HOO*}} = G(\mathrm{HOO*}) - G(*) - 2G(\mathrm{H_2O}) + 3/2G(\mathrm{H_2}) \qquad Eq.\ \mathrm{S3}$$

where *G*(HOO*), *G*(*) are the free energies of adsorption structure and clean surface, respectively. *G*(H_2O), *G*(H_2) is the free energy of H_2O(l) and H_2(g), respectively.

Supporting figures

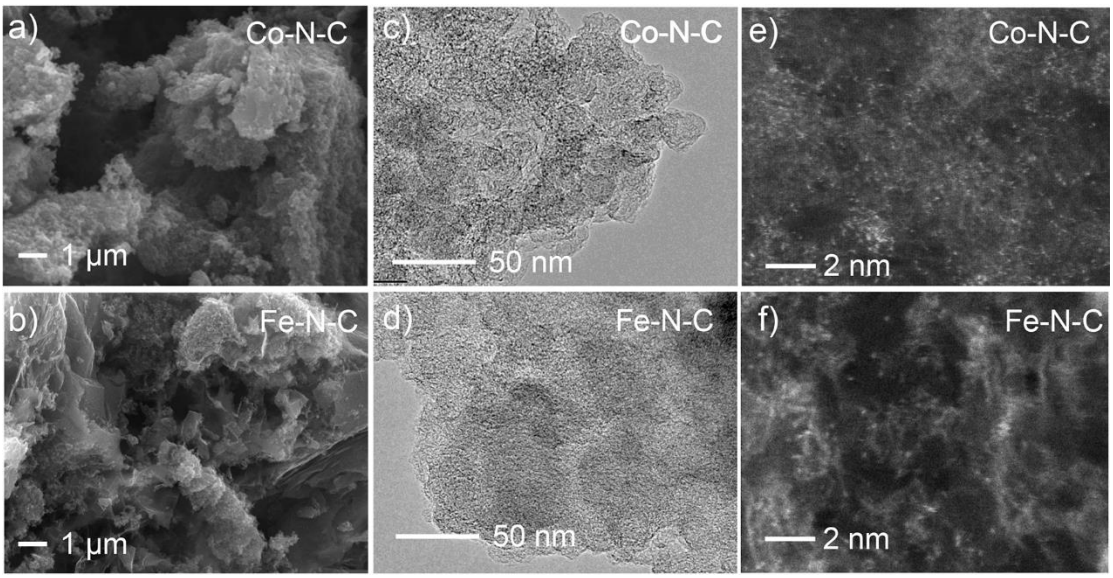

Figure S1. Characterization of the Co-N-C and Fe–N–C catalysts. (a, b) SEM micrographs; (c, d) transmission electron microscopy (TEM) images, and (e, f) scanning transmission electron microscopy (STEM) images of the Co-N-C and Fe-N-C catalysts.

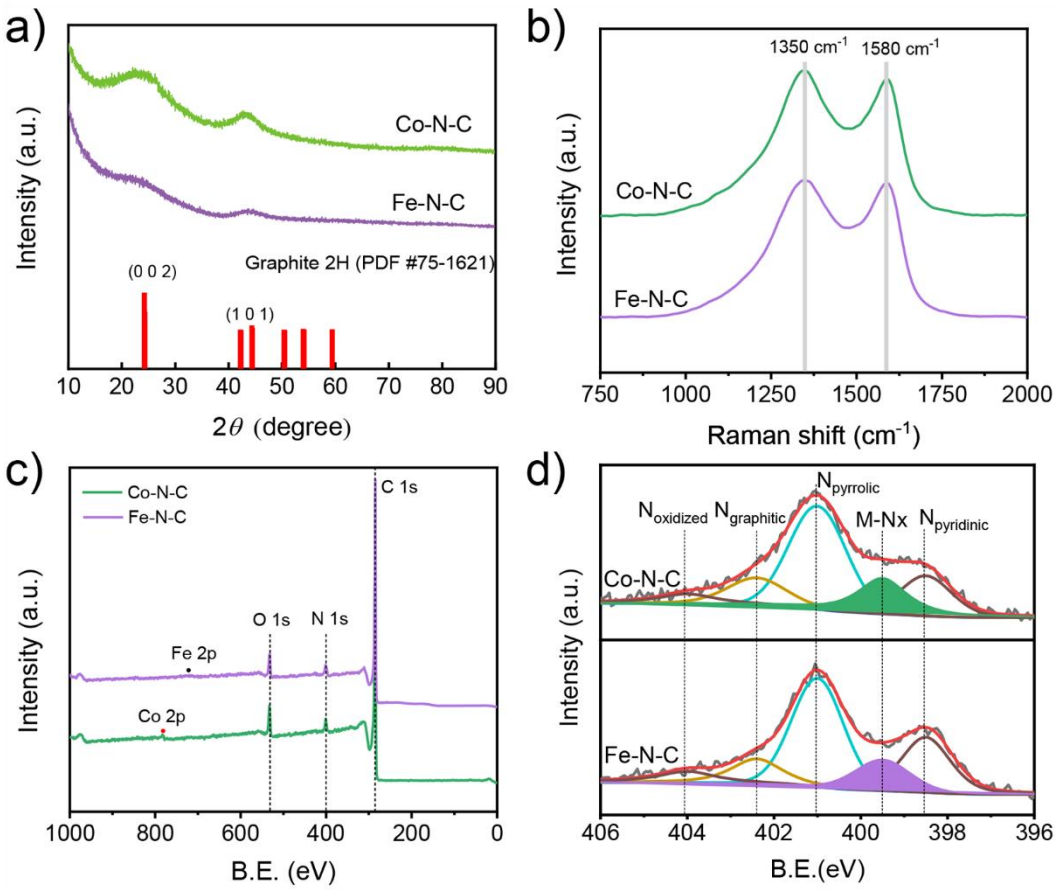

Figure S2. Characterization of the Co-N-C and Fe–N–C catalysts. (a) XRD patterns, (b) Raman spectra, (c) survey XPS spectra, and (d) N1s XPS spectra of the Co-N-C and Fe-N-C catalysts.

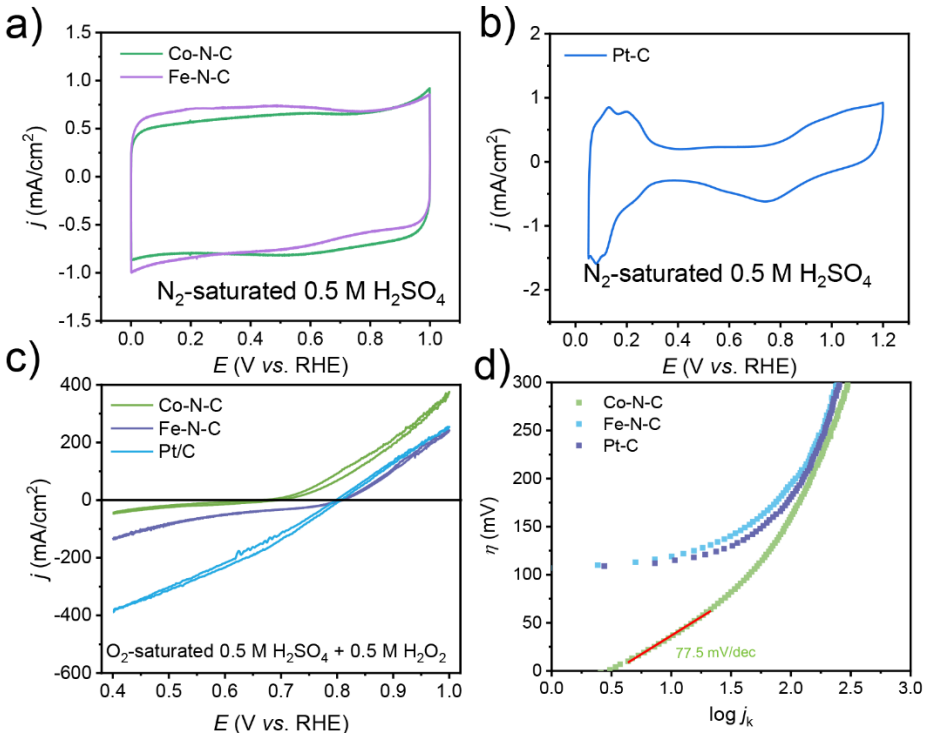

Figure S3. Cyclic voltammograms (CVs) of the (a) Co-N-C, Fe-N-C, and (b) Pt-C catalysts in RDE system. Scan rate: 50 mV/s. The loading of Co-N-C and Fe-N-C on the RDE was *ca*. 0.1 mg/cm^2. The Pt-C loading on the RDE was *ca*. 0.1 mg/cm^2 (0.02 mg$_{Pt}$/cm^2). HPOR performance comparisons. (c) Cyclic voltammetry curves recorded in 0.5 M H_2SO_4 and 0.5 M H_2O_2 by an RDE system. Rotation rate: 900 rpm; scan rate: 50 mV/s; temperature: 25 °C; Co-N-C and Fe-N-C catalysts loading: 0.1 mg/cm^2; Pt-C catalyst loading: 0.1 mg/cm^2. (d) Tafel plot of the current density (*j*) for the HPOR measured with the Co-N-C catalyst.

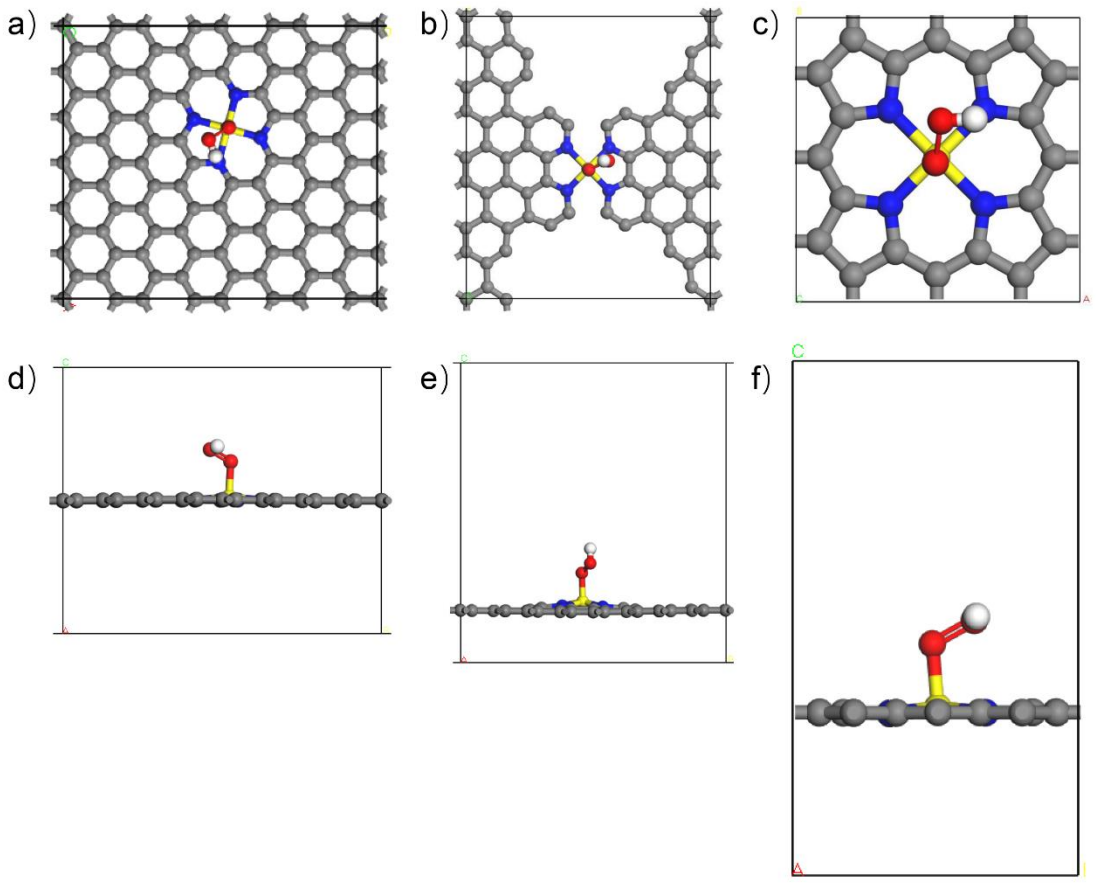

Figure S4. The optimized adsorption structures of HOO* intermediate for (a, d) Co-$N_{4\text{-pyridinic}}$, (b, e) Co-$N_{2+2\text{-pyridinic}}$, (c, f) Co-$N_{4\text{-pyrrolic}}$.

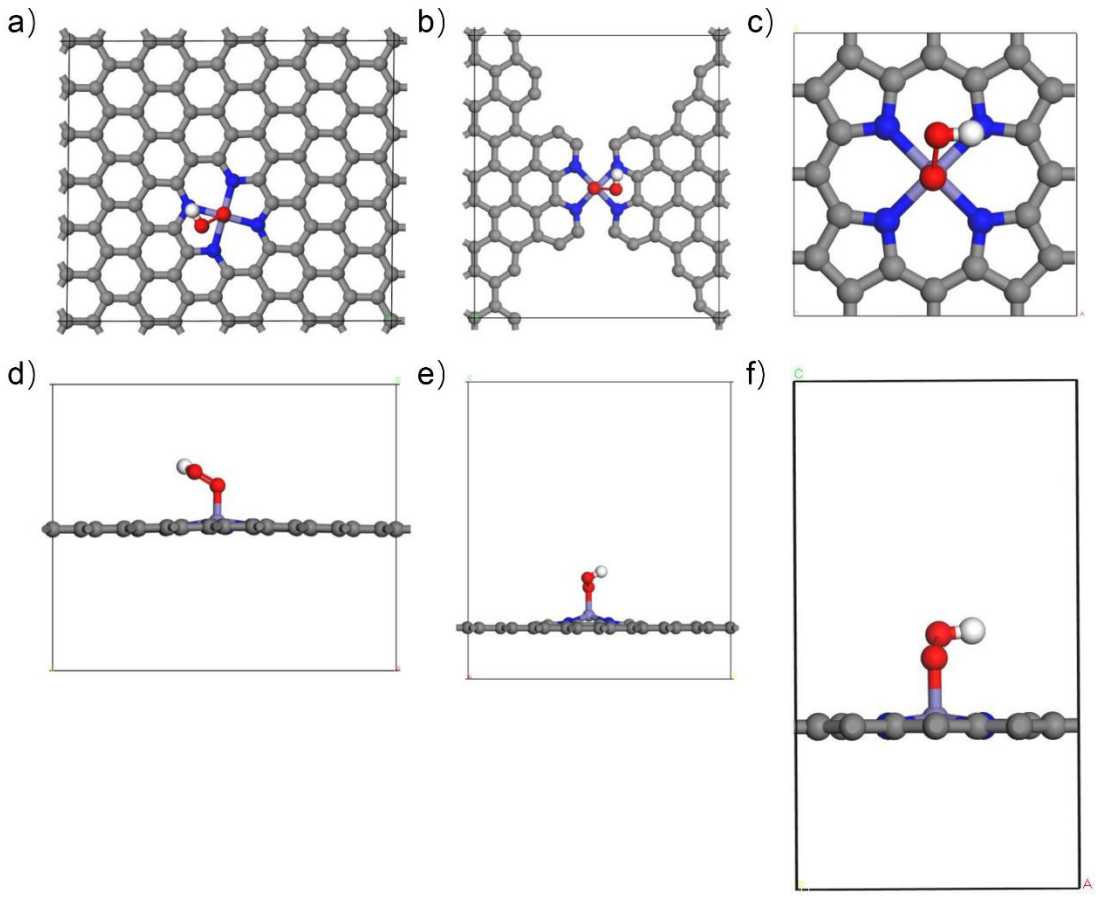

Figure S5. The optimized adsorption structures of HOO* intermediate for (a, d) Fe-$N_{4\text{-pyridinic}}$, (b, e) Fe-$N_{2+2\text{-pyridinic}}$, (c, f) Fe-$N_{4\text{-pyrrolic}}$.

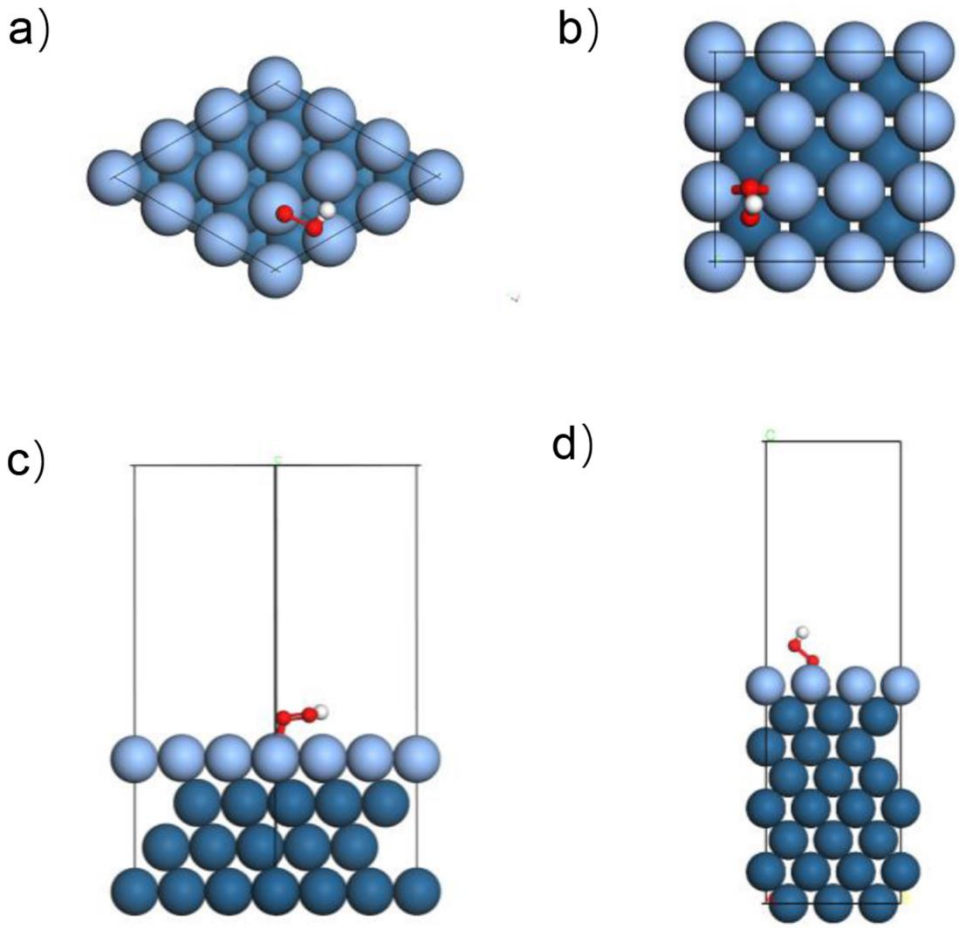

Figure S6. The optimized adsorption structures of HOO* intermediate for (a, c) Pt (111), and (b, d) Pt (100).

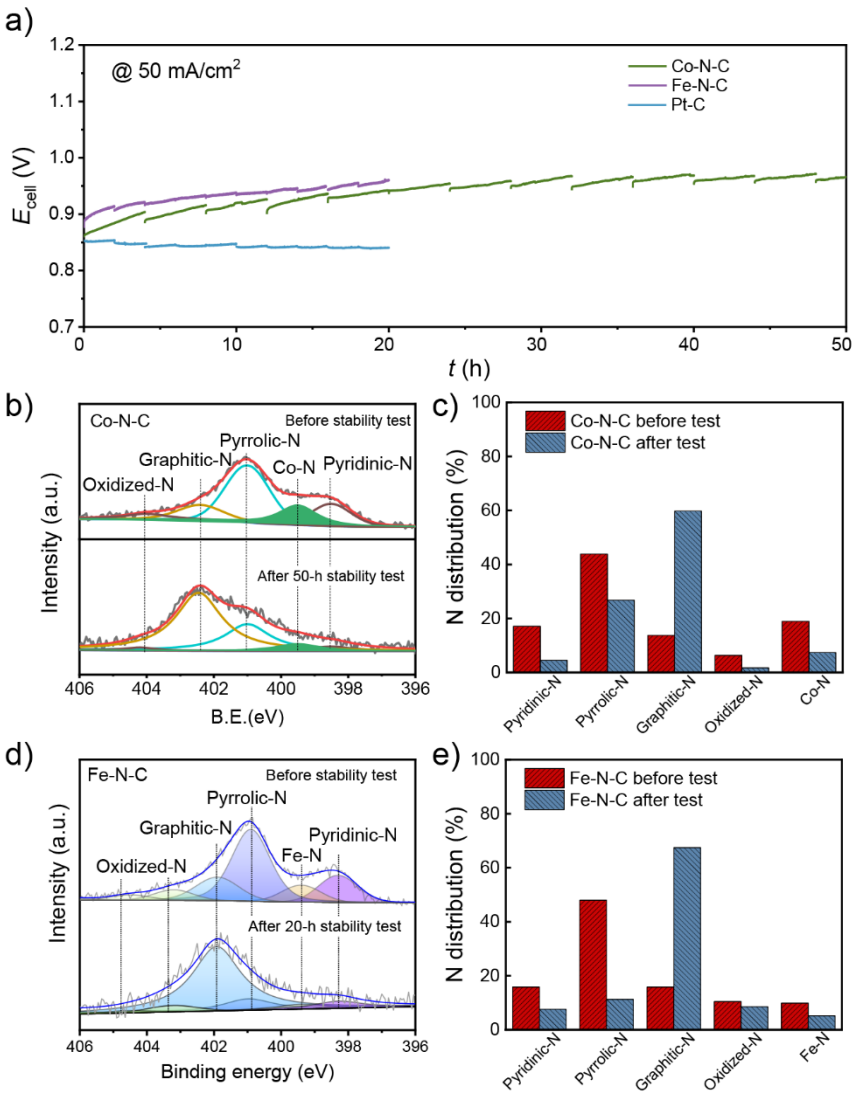

Figure S7. (a) The Co-N-C, Fe-N-C, and Pt-C catalysts were tested for stability of continuous H_2 generation at a fixed current density of 50 mA/cm^2.[1,2] High-resolution N 1s XPS spectra and N distribution as different species in the (b, c) Co–N–C catalyst after a 50-h stability test, and (d, e) in the Fe-N-C catalyst after a 20-h stability test.[1,2]

Note. The HPEL stability was evaluated using the galvanostatic method at a fixed current density of 50 mA/cm^2. The flow rate of the anolyte solution was 50 mL/min. And the solution was replaced with fresh solutions every two hours (Fe-N-C and Pt-C catalyst) or four hours (Co-N-C catalyst).[1,2]

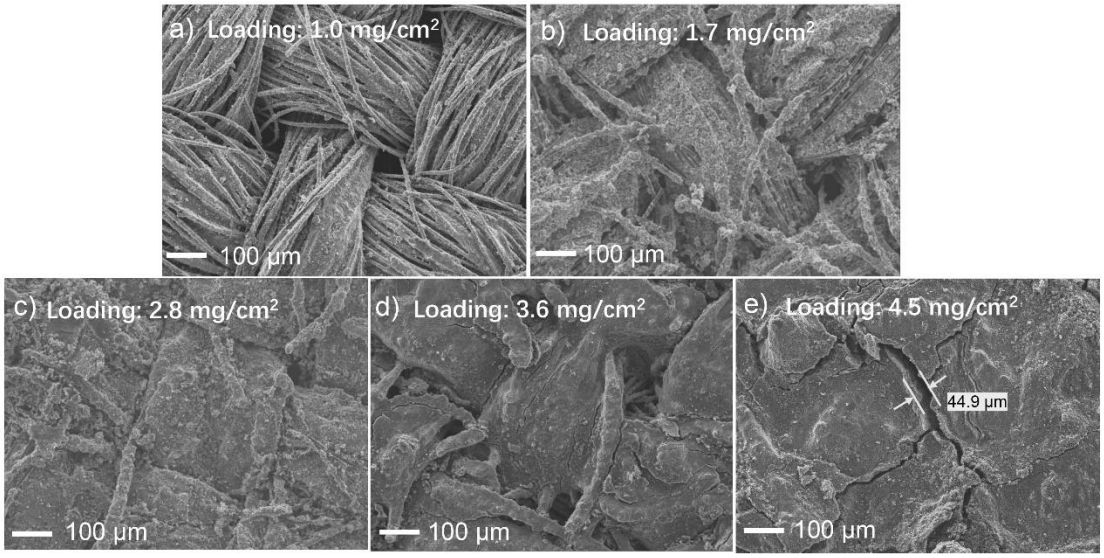

Figure S8. The SEM images of the MEA with the Co-N-C catalyst loadings of (a) 1.0, (b) 1.7, (c) 2.8, (d) 3.6 and (e) 4.5 mg/cm^2.

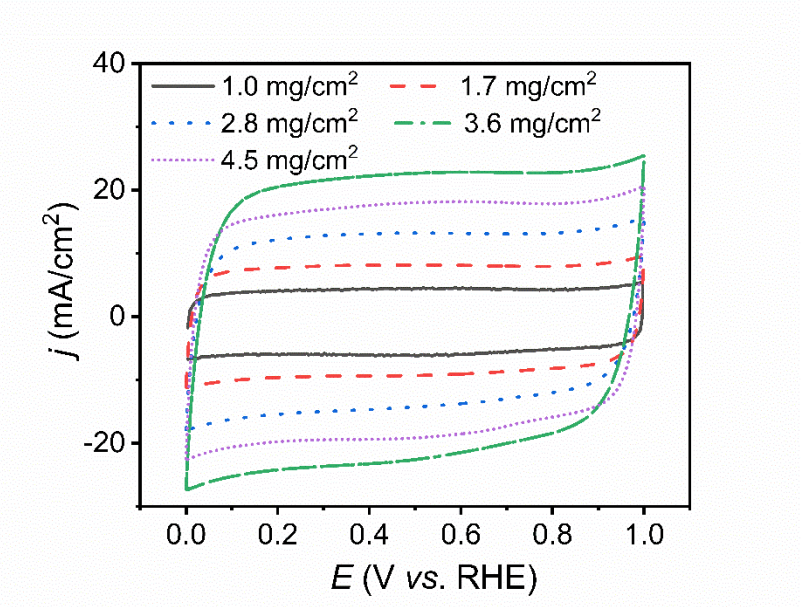

Figure S9. Anode CV curves of PEM HPELs with Co-N-C catalyst loadings of 1.0, 1.7, 2.8, 3.6, and 4.5 mg/cm^2. Scan rate: 50 mV/s. Cell temperature: 25 °C.

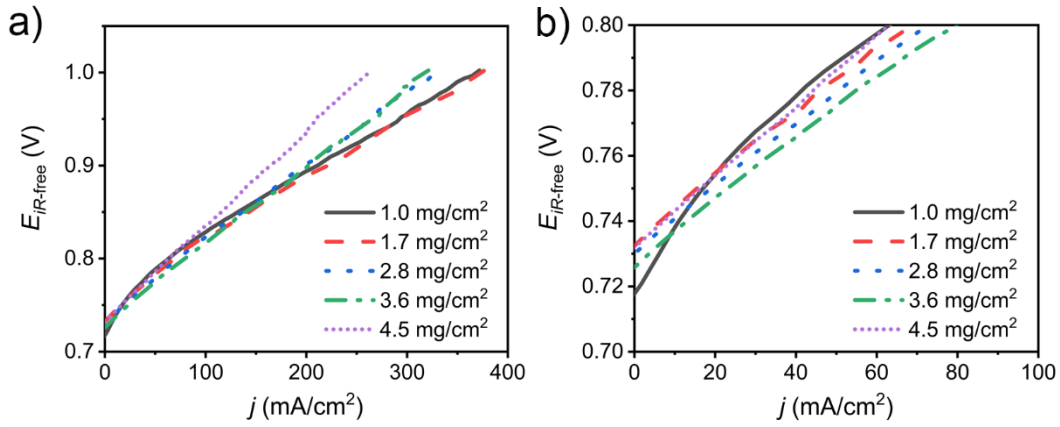

Figure S10. Polarization curves of PEM HPELs with different loadings of Co-N-C catalyst at anode within the voltage range of (a) 0.7 to 1.0 $V_{iR\text{-free}}$, and (b) 0.7 to 0.8 $V_{iR\text{-free}}$. Cell temperature: 25 °C; cathode catalyst loading: 0.2 mg_{Pt}/cm^2; membrane: NR 212 (50.8 μm).

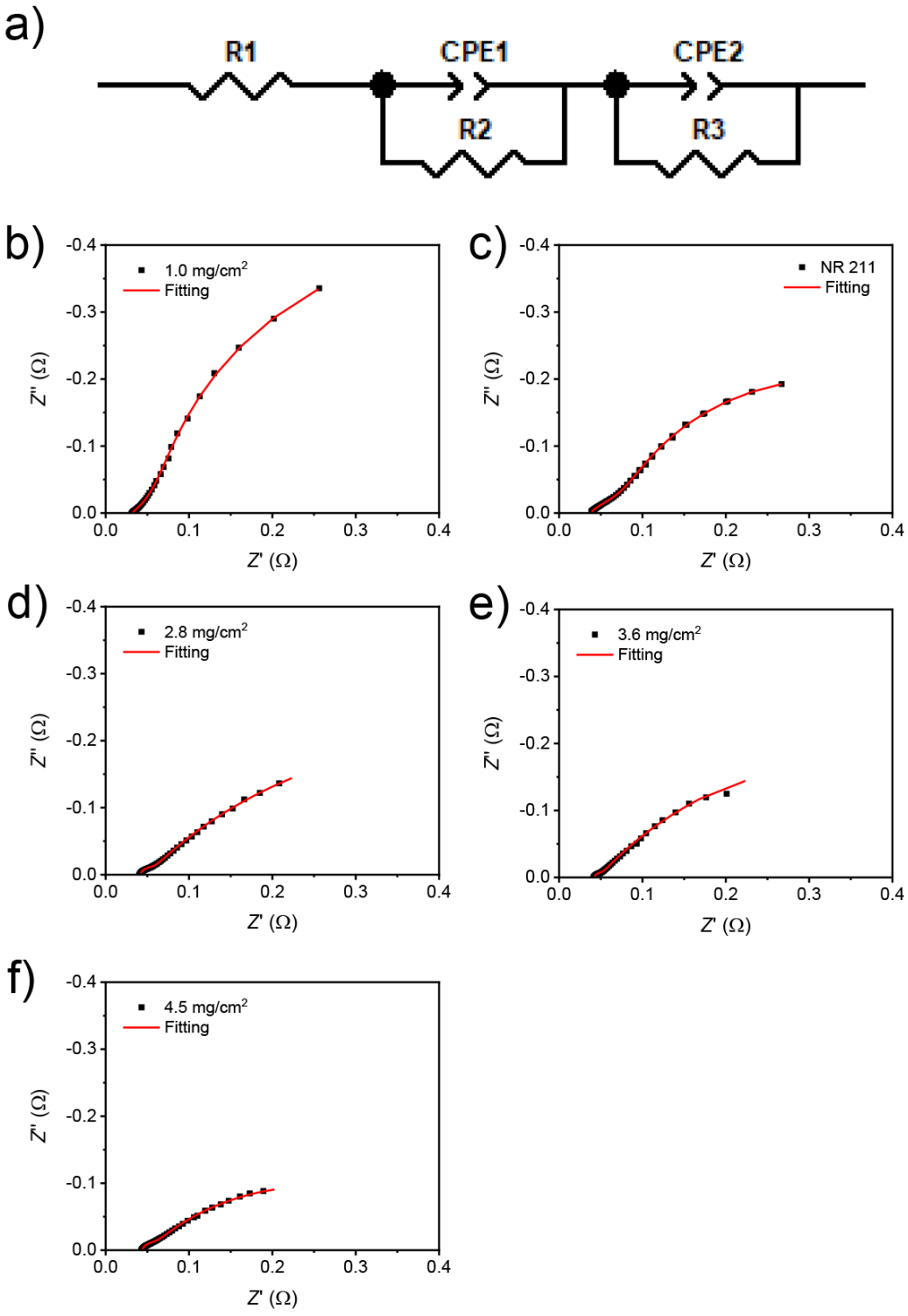

Figure S11. a) Equivalent circuit, and b-f) bode plots of PEM HPELs measured at OCV with different anode catalyst loadings of Co-N-C catalyst. Cell temperature: 25 °C; cathode catalyst loading: 0.2 mg_{Pt}/cm^2; membrane: NR 212 (50.8 μm).

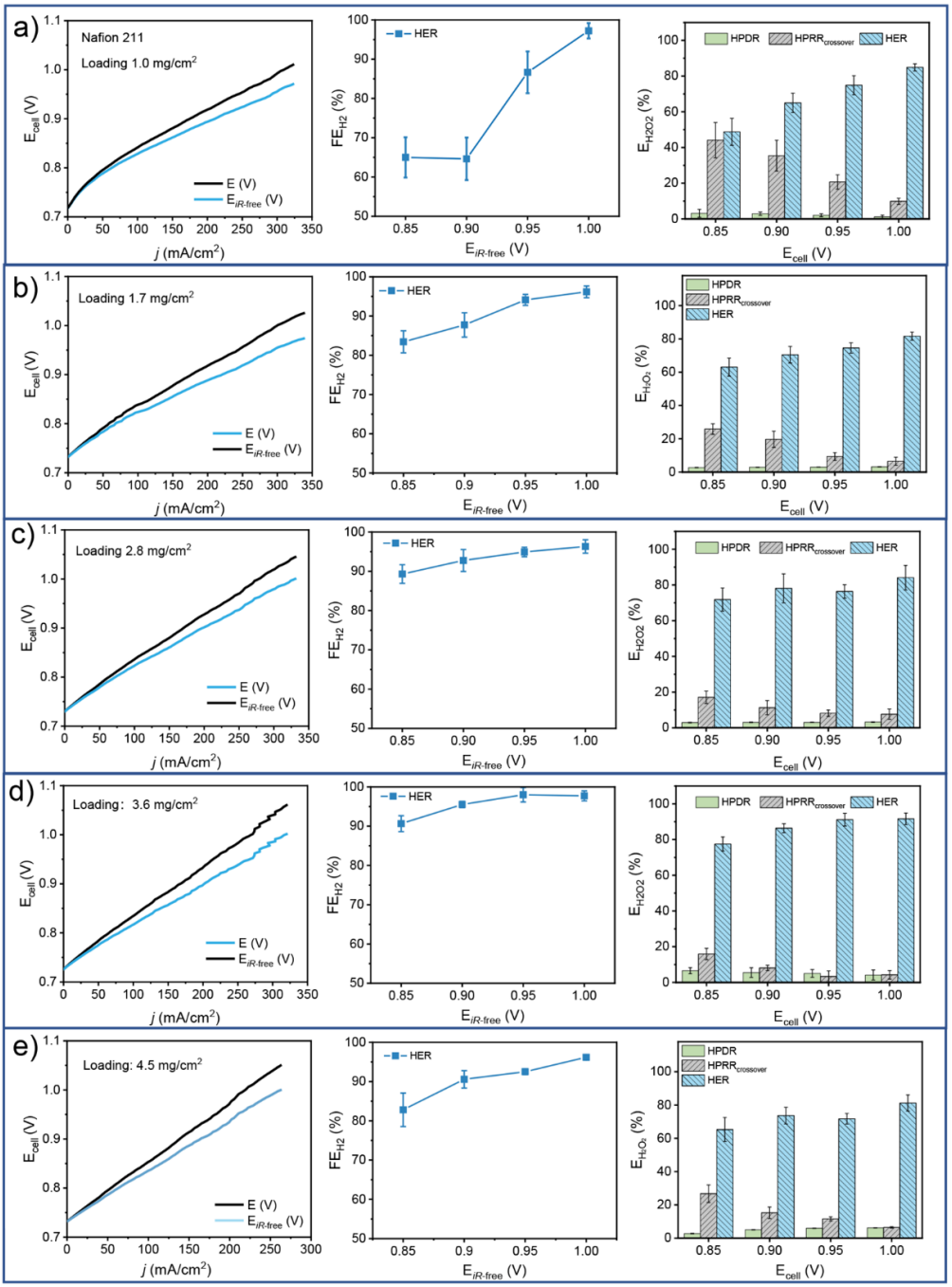

Figure S12. Performance of PEM HPELs with different Co-N-C catalyst loadings of (a)1.0, (b)1.7, (c) 2.8, (d) 3.6, and (e) 4.5 mg/cm^2, including the polarization curves (LSV), Faradaic efficiency (FE_{H2}), and the efficiency of H_2O_2 (E_{H2O2}) consumed for H_2 generation ($E_{H2O2\text{-}HER}$), disproportionation ($E_{H2O2\text{-}HPDR}$), and crossover ($E_{H2O2\text{-}HPRRcross}$) at various $E_{iR\text{-}free}$. Cell temperature: 25 °C; cathode catalyst loading: 0.2 mg_{Pt}/cm^2; membrane: NR 212 (50.8 μm).

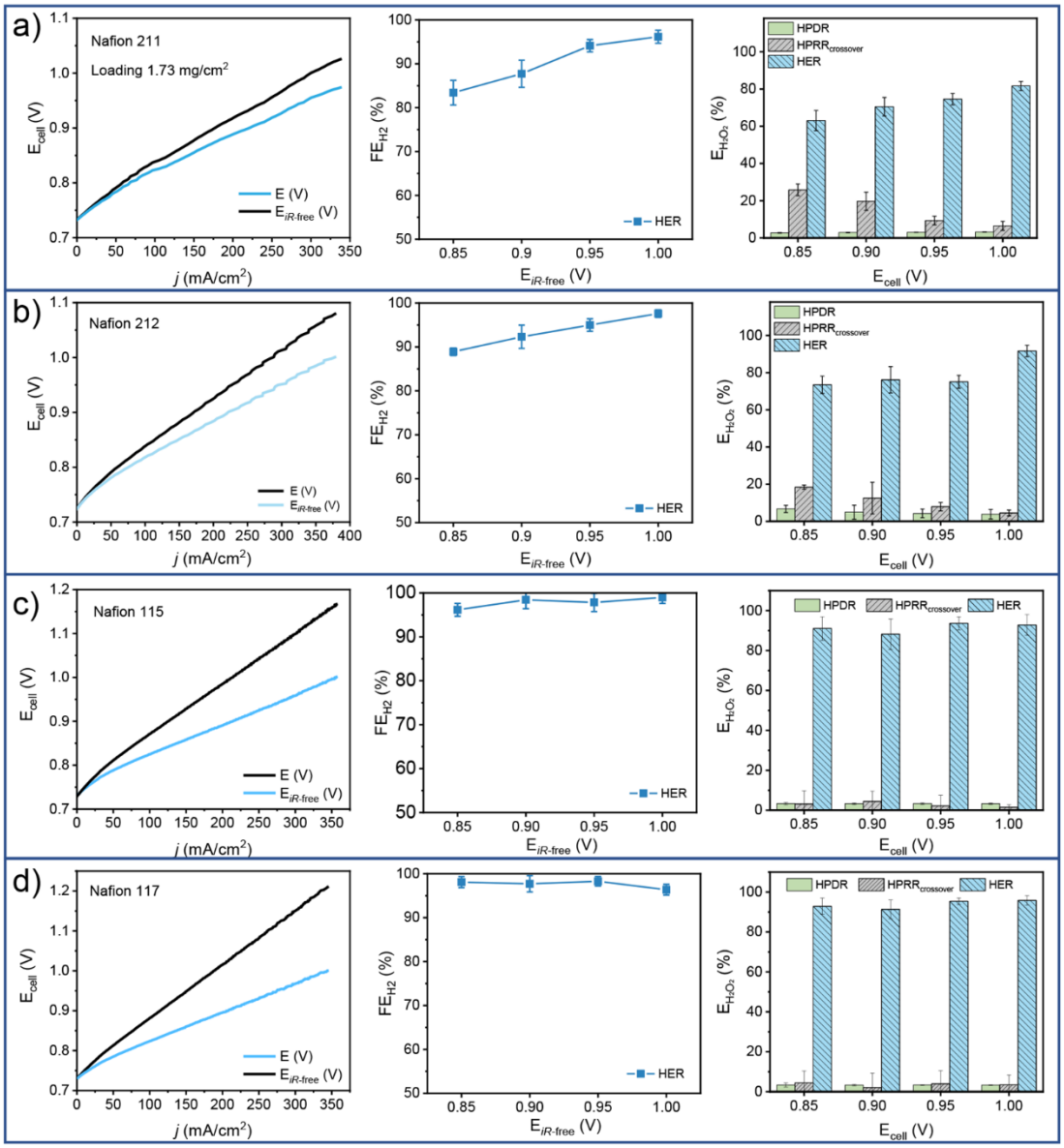

Figure S13. Performance of PEM HPELs with different membrane thicknesses of (a) 25.4 μm (NR 211), (b) 50.8 μm (NR 212), (c) 127.0 μm (NR 115), and (d) 183.0 μm (NR 117), including the polarization curves (LSV), faradaic efficiency (FE_{H2}), and the efficiency of H_2O_2 (E_{H2O2}) consumed for H_2 generation ($E_{H2O2\text{-}HER}$), disproportionation ($E_{H2O2\text{-}HPDR}$), and crossover ($E_{H2O2\text{-}HPRRcross}$) at various $E_{iR\text{-}free}$. Cell temperature: 25 °C; cathode catalyst loading: 0.2 mg_{Pt}/cm^2; anode Co-N-C catalyst loading: 1.7 mg/cm^2.

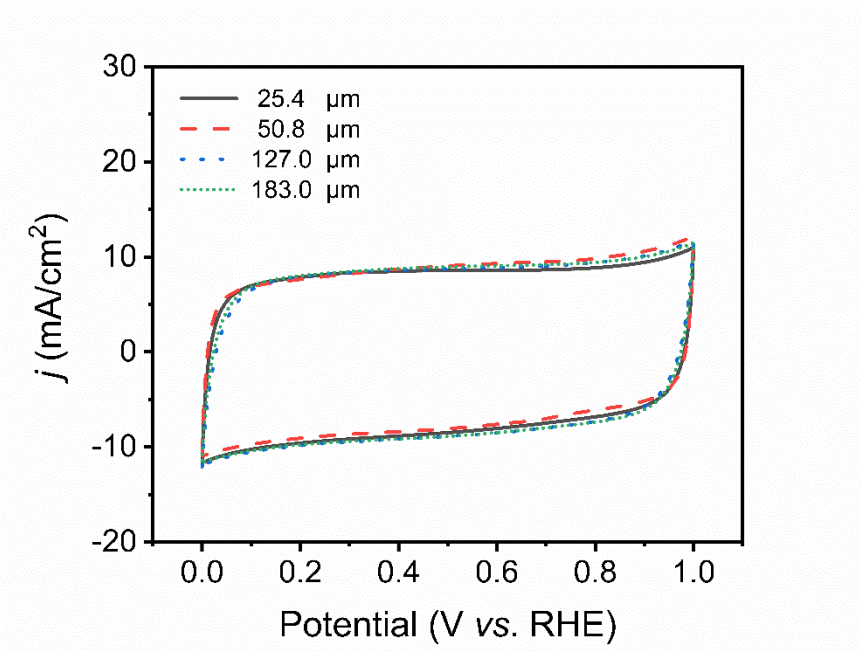

Figure S14. Anode CV curves of PEM HPELs with different membrane thicknesses. Cell temperature: 25 °C; cathode catalyst loading: 0.2 mg_{Pt}/cm^2; anode Co-N-C catalyst loading: 1.7 mg/cm^2.

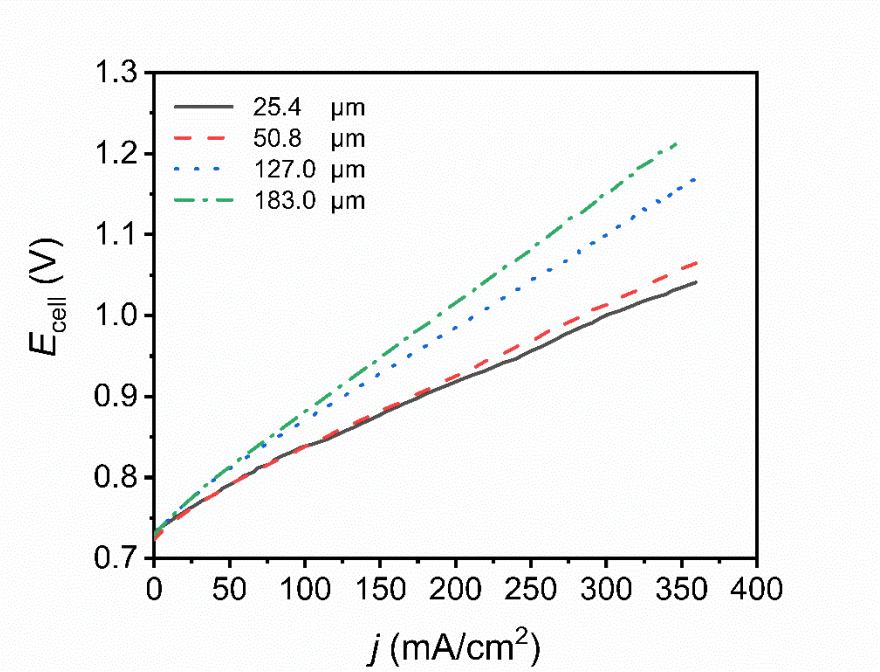

Figure S15. Polarization curves of PEM HPELs with different membrane thickness. Cell temperature: 25 °C; cathode catalyst loading: 0.2 mg_{Pt}/cm^2; anode Co-N-C catalyst loading: 1.7 mg/cm^2.

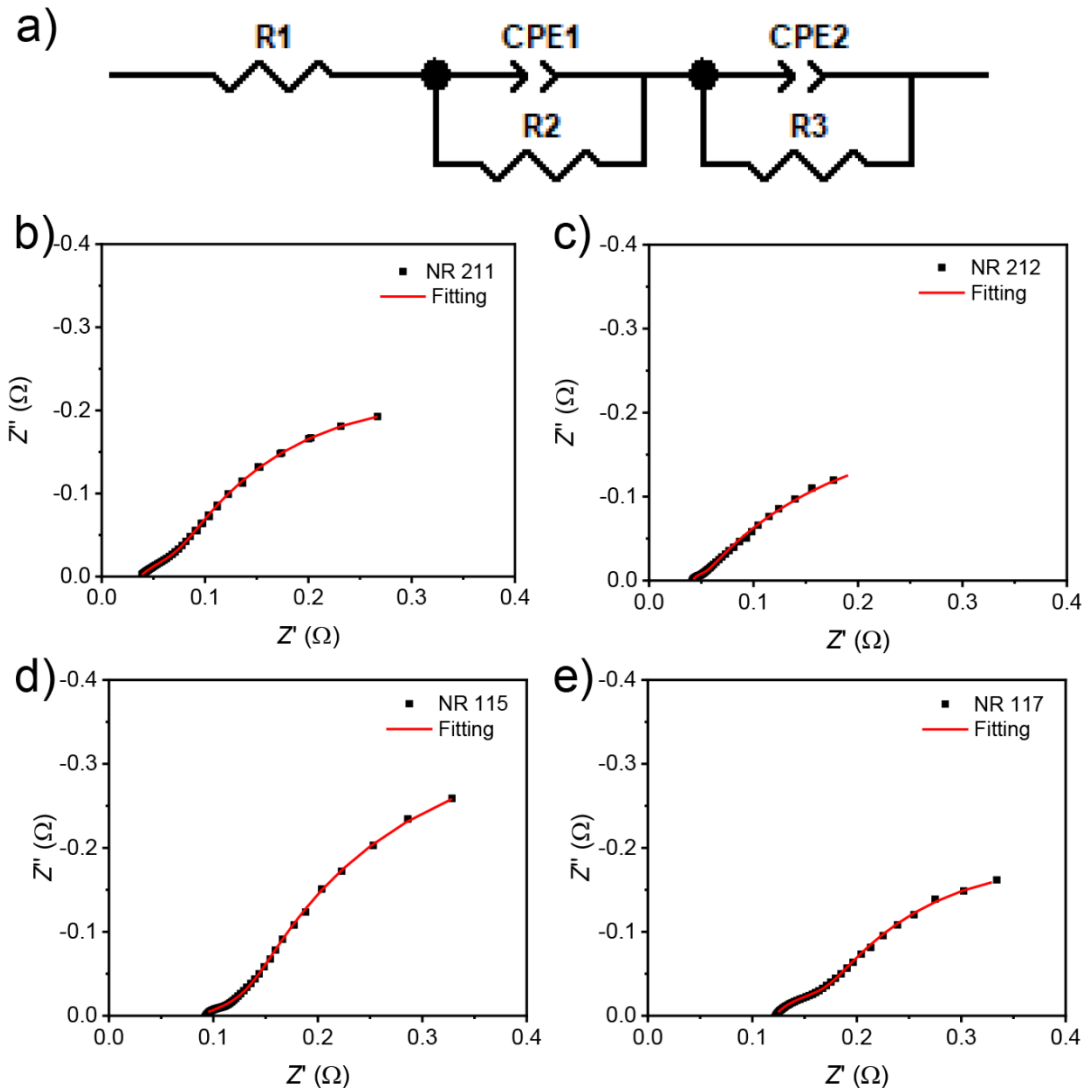

Figure S16. a) Equivalent circuit, and b-e) bode plots at OCV with different membrane thicknesses. Cell temperature: 25 °C; cathode catalyst loading: 0.2 mg_{Pt}/cm^2; anode Co-N-C catalyst loading: 1.7 mg/cm^2.

Table S1. Comparison of various types of electrochemical energy storage systems.

Energy storage System	Technology paths	Main feature	Working Temperature (°C)	Voltage efficiency	Technical status	Ref
H_2-water cycle	UR-PEMFC	Noble metal catalyst	20-100	40%-50%	Mautre	12-19
	UR-AEMFC	Non-noble metal catalyst	20-120	30%-40%	Developing	
	UR-SOFC	High-temperature operation	500-1000	60%-80%	Developing	
Ammonia-N_2 cycle	NH_3-O_2 fuel cell *vs*. Ammonia synthesis	Alleviate safety issues	20-80	22%	Early stage	20-23
H_2O_2-water cycle	Direct H_2O_2 Fuel Cell *vs*. H_2O_2 synthesis	H_2O_2 as an energy carrier	20-40	——	Early stage	24-26
Rechargeable metal-ion batteries	Sodium-ion battery	Cheaper and abundant	-20-80	80%-90%	Developing	27, 28
	Potassium-ion battery	High electrical conductivity	0-55	80%-90%	Developing	
	Lithium-ion battery	High energy density and long cycle life	0-40	80%-90%	Mautre	
Flow batteries	Vanadium redox flow battery	High energy efficiency and long cycle life,	5-45	60%-70%	Mautre	29-31
	Zinc–bromine flow battery	Environmentally friendly	-30-50	70%-75%	Developing	
	Iron–chromium flow battery	High safety and low cost	-40-70	70%-75%	Developing	
H_2-H_2O_2 cycle	H_2-O_2 fuel cell *vs*. H_2O_2 electrolyzer	H_2O_2 as an energy carrier and non-noble metal catalyst	-20-80	90%	Early stage	This work

Table S2. The binding free energies of HOO* intermediate for Fe-N-C, Pt(111) and Pt(100) surfaces (U = 0 V vs. CHE). HOO* intermediate dissociates spontaneously on Pt(110) surface.

	Co-N$_{4\text{-pyridinic}}$	**Co-N$_{2+2\text{-pyridinic}}$**	**Co-N$_{4\text{-pyrrolic}}$**
ΔG_{HOO*}	3.50	3.66	4.16
	Fe-N$_{4\text{-pyridinic}}$	**Fe-N$_{2+2\text{-pyridinic}}$**	**Fe-N$_{4\text{-pyrrolic}}$**
ΔG_{HOO*}	3.29	3.13	3.72
	Pt(111)	**Pt(100)**	**Pt(110)**
ΔG_{HOO*}	3.77	3.28	/

References

1. Yang, J.; Ding, R.; Liu, C.; Liu, S.; Xu, Q.; Chen, L.; Chen, J.; Li, J.; Yin, X., Highly Efficient Unitized Regenerative Hydrogen Peroxide Cycle Cell with Ultralow Overpotential for Renewable Energy Storage. J. Power Sources, 2022, **545,** 231948.

2. Liu, C.; Ding, R.; Yang, J.; Liu, S.; Chen, L.; Xu, Q.; Li, J.; Yin, X., Low-Voltage Hydrogen Peroxide Electrolyzer for Highly Efficient Power-to-Hydrogen Conversion. ACS Sustain. Chem. Eng., 2023, **11,** 2599-2606.

3. Perdew, J. P.; Burke, K. ; Ernzerhof, M., Generalized Gradient Approximation Made Simple. *Phys. Rev. Lett.* 1996, **77,** 3865−3868.

4. Kresse, G.; Furthmüller, J., Efficiency of Ab-Initio Total Energy Calculations for Metals and Semiconductors Using a Plane-Wave Basis Set. *Comput. Mater. Sci.* 1996, **6,** 15−50.

5. Kresse, G.; Furthmüller, J., Efficient Iterative Schemes for Ab Initio Total-Energy Calculations Using a Plane-Wave Basis Set. *Phys. Rev. B: Condens. Matter Mater. Phys*. 1996, **54,** 11169−11186.

6. Blöchl, P. E., Projector Augmented-wave Method. *Phys. Rev. B: Condens. Matter Mater. Phys.* 1994, **50,** 17953−17979.

7. Kresse, G.; Joubert, D., From Ultrasoft Pseudopotentials to the Projector Augmented-Wave Method. *Phys. Rev. B: Condens. Matter Mater. Phys.* 1999, **59,** 1758−1775.

8. Grimme, S.; Antony, J.; Ehrlich, S.; Krieg, H., A Consistent and Accurate Ab Initio Parametrization of Density Functional Dispersion Correction (DFT-D) for the 94 Elements H-Pu. *J. Chem. Phys.* 2010, **2,** 154104.

9. Nørskov, J. K.; Rossmeisl, J.; Logadottir, A.; Lindqvist, L., Origin of the Overpotential for Oxygen Reduction at a Fuel Cell Cathode. *J. Phys. Chem. B* 2004, **108,** 17886-17892.

10. He, Z.; Hanselman, S.; Chen, Y.; Koper, M. T. M.; Calle-Vallejo, F., Importance of Solvation for the Accurate Prediction of Oxygen Reduction Activities of Pt-Based Electrocatalysts. *J. Phys. Chem. Lett.* 2017, **8,** 2243–2246.

11. Calle-Vallejo, F.; Martínez, J. I.; Rossmeisl, J., Density Functional Studies of Functionalized Graphitic Materials with Late Transition Metals for Oxygen Reduction Reactions. *Phys. Chem. Chem. Phys*. 2011, **13,** 15639−15643.

12. Nikolaidis, P.; Poullikkas, A., A Comparative Overview of Hydrogen Production Processes. *Renew. Sust. Energ. Rev.*, 2017, **67,** 597-611.

13. Pivovar, B.; Rustagi, N.; Satyapal, S., Hydrogen at Scale (H_2 @Scale): Key to a Clean, Economic, and Sustainable Energy System. *J. Electrochem. Soc.*, 2018, **27,** 47-52.

14. Barreto, L.; Makihira, A.; Riahi, K., The Hydrogen Economy in the 21st Century: A Sustainable Development Scenario. *Int. J. Hydrog. Energy*, 2003, **28,** 267-284.

15. Du, N.; Roy, C.; Peach, R.; Turnbull, M.; Thiele, S.; Bock, C., Anion-Exchange Membrane Water Electrolyzers. *Chem. Rev.*, 2022, **122,** 11830-11895.

16. Jin, H.; Ruqia, B.; Park, Y.; Kim, H. J.; Oh, H.-S.; Choi, S.-I.; Lee, K., Nanocatalyst Design for Long-Term Operation of Proton/Anion Exchange Membrane Water Electrolysis. *Adv. Energy Mater.*, 2021, **11,** 2003188.

17. Lee, B.; Heo, J.; Kim, S.; Sung, C.; Moon, C.; Moon, S.; Lim, H., Economic

Feasibility Studies of High Pressure Pem Water Electrolysis for Distributed H_2 Refueling Stations. *Energy Convers. Manag*, 2018, **162,** 139-144.

18. Miller, H. A.; Bouzek, K.; Hnat, J.; Loos, S.; Bernäcker, C. I.; Weißgärber, T.; Röntzsch, L.; Meier-Haack, J., Green Hydrogen from Anion Exchange Membrane Water Electrolysis: A Review of Recent Developments in Critical Materials and Operating Conditions. *Sustain. Energy Fuels*, 2020, **4,** 2114-2133.

19. Li, D.; Motz, A. R.; Bae, C.; Fujimoto, C.; Yang, G.; Zhang, F.-Y.; Ayers, K. E.; Kim, Y. S., Durability of Anion Exchange Membrane Water Electrolyzers. *Energy Environ. Sci.*, 2021, **14,** 3393-3419.

20. Xue, X.; Chen, R.; Yan, C.; Zhao, P.; Hu, Y.; Zhang, W.; Yang, S.; Jin, Z., Review on Photocatalytic and Electrocatalytic Artificial Nitrogen Fixation for Ammonia Synthesis at Mild Conditions: Advances, Challenges and Perspectives. *Nano Res.*, 2019, **12,** 1229-1249.

21. Singh, A. R.; Rohr, B. A.; Schwalbe, J. A.; Cargnello, M.; Chan, K.; Jaramillo, T. F.; Chorkendorff, I.; Nørskov, J. K., Electrochemical Ammonia Synthesis—The Selectivity Challenge. *ACS Cat*. 2017, **7,** 706-709.

22. Cui, X.; Tang, C.; Zhang, Q., A Review of Electrocatalytic Reduction of Dinitrogen to Ammonia under Ambient Conditions. *Adv. Energy Mater*., 2018, **8,** 1800369.

23. Canfield, D. E.; Glazer, A. N.; Falkowski, P. G., The Evolution and Future of Earth's Nitrogen Cycle. *Science*, 2010, **330,** 192-196.

24. Sanli, A. E.; Aytaç, A., Response to Disselkamp: Direct Peroxide/Peroxide Fuel Cell as a Novel Type Fuel Cell. *Int. J. Hydrog. Energy*, 2011, **36,** 869-875.

25. Sanlı, A. E., A Possible Future Fuel Cell: The Peroxide/Peroxide Fuel Cell. *Int. J. Energy Res.*, 2013, **37,** 1488-1497.

26. Fukuzumi, S.; Yamada, Y.; Karlin, K. D., Hydrogen Peroxide as a Sustainable Energy Carrier: Electrocatalytic Production of Hydrogen Peroxide and the Fuel Cell. *Electrochim. Acta*, 2012, **82,** 493-511.

27. Soltani, N.; Bahrami, A.; Giebeler, L.; Gemming, T.; Mikhailova, D., Progress and Challenges in Using Sustainable Carbon Anodes in Rechargeable Metal-Ion Batteries *Prog. Energy Combust. Sci.*, 2021, **87,** 100929.

28. Liang, Y.; Dong, H.; Aurbach, D.; Yao, Y., Current Status and Future Directions of Multivalent Metal-Ion Batteries. *Nat. Energy*, 2020, **5,** 646-656.

29. Winsberg, J.; Hagemann, T.; Janoschka, T.; Hager, M. D.; Schubert, U. S., Redox-Flow Batteries: From Metals to Organic Redox-Active Materials. *Angew. Chem. Int. Ed*., 2017, **56,** 686-711.

30. Weber, A. Z.; Mench, M. M.; Meyers, J. P.; Ross, P. N.; Gostick, J. T.; Liu, Q., Redox Flow Batteries: A Review. *J Appl Electrochem*, 2011, **41,** 1137-1164.

31. Gencten, M.; Sahin, Y., A Critical Review on Progress of the Electrode Materials of Vanadium Redox Flow Battery. *Int. J. Energy Res*., 2020, **44,** 7903-7923.